Time-resolved studies of Warm Dense Titanium:
A Bayesian search of coupling parameters

Sebastião Antunes*

Instituto Superior Técnico, Universidade de Lisboa

1. INTRODUCTION

Warm dense matter (WDM) exists at the intersection of condensed matter and classical plasma physics. It is created in Inertial Confinement Fusion (ICF) experiments - when a driving laser heats up and compresses a solid fuel target [1] - and is present in astrophysical objects such as gas giants, brown and white dwarfs, and low-mass stars [2–4]. Femtosecond laser technology provides many practical applications for material modification, including the promising technique of laser ablation that enables precise micro and nano machining [5], and produces WDM before macroscopic expansion of the ablating material.

WDM states are characterized by temperatures ranging from 0.1 to 100 eV and roughly solid densities (0.1 to 10 times ρ_{solid}). Having thermal and Fermi energies close to one another, these states of matter are placed in between the quantum regime of strong degeneracy and the classical regime of non-degeneracy. Atomic or ionic binding energies also close to the average thermal energy ($\Gamma = \langle E_{\text{Coulomb}} \rangle / \langle E_{\text{kinetic}} \rangle \sim 1$) makes WDM states sit in the transition between solid, liquid gas, and plasma [6].

In dense Coulomb plasmas, we cannot neglect the quantum nature of its electrons. In equilibrium conditions, the spatial width of the most likely spatial region for the electron to be in is roughly given by the thermal length $\Lambda_e = \sqrt{2\pi\hbar/(m_a k_B T)}$ [7]. The mean particle distance, on the other hand, can be written as $d_e \propto 1/\sqrt[3]{n_e}$. In WDM, the inter-atomic distance is of the order of the thermal length, i.e $n_e \Lambda_e \approx 1$. In this case, we have to start taking the indistinguishability of the plasma particles into account.

An important phenomenon in plasmas and solids alike, affected by Λ_e is the Coulomb screening of the potential of an electric charge, as it describes how induced fields are shielded by surrounding charges. By solving the linearized Vlasov equation for, in the static limit we obtain the effective Coulomb potential [7]:

$$\Phi^{\text{eff}}(\mathbf{k}, 0) = \frac{4\pi e_0}{k^2 + \kappa^2} \longrightarrow \Phi^{\text{eff}}(r) = \frac{e_0}{r} \exp(-r/r_0). \quad (1)$$

where κ^2 is the inverse screening radius (r_0) and is defined in terms of the electronic number density and temperature.

The expression above makes clear that the long-range nature of the Coulomb potential of the point charge is suppressed by the polarized plasma particles. The potential mediating the interaction between two constituent plasma particles is the Coulomb one, up to a radius of $\approx r_0$ and decays exponentially for larger radii. Valuable physical insight is hidden, as usual, in the limiting cases. When $n_e \Lambda_e^3 \ll 1$, i.e., in the non-degenerate regime, the well-known Debye screening length is obtained. In the

strongly degenerate regime, where $n_e \Lambda_e^3 \gg 1$, on the other hand, the Thomas-Fermi screening length is recovered. The fact that the former is much stronger than the latter suggests that many-body effects - responsible for the screening - are much stronger in cold solids than plasmas.

To uncover the temperature-density boundary between the two regimes we turn to more ad hoc arguments. We can now define the Warm Dense region in a phase space diagram. We expect quantum effects to dominate, namely strong correlations and degeneracy effects of the electrons, where $\Gamma > 1$ and $n_e \Lambda_e > 1$. These boundaries push our regime to the hotter and denser side of the diagram. At high enough densities, however, full ionization will take place and the quantum correlations lose importance. This places an upper bound to our regime at the line $r_s = 1$, with r_s called the Brueckner parameter, and being the ratio between the mean particle distance and the Bohr radius.
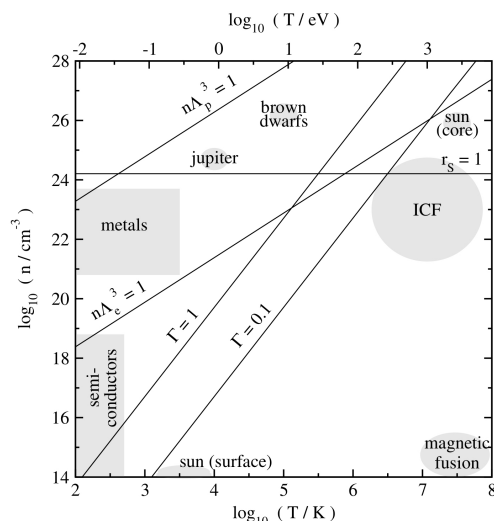

FIG. 1: Temperature-density plane with several adimensional parameters plotted, for the equilibrium case, along with demarcations of different zones of physical and technological interest. From [7].

Since WDM sits between so-many different regimes, appropriate benchmarking of theoretical models against the experiments is sorely needed. Creating and probing such states in laboratory conditions, however, comes with its own set of challenges.

A common way of creating WDM is with X-ray sources or proton beams than penetrate inside solid density material beyond the skin depth, depositing their energy in μm, length scales before significant hydrodynamic expansion kicks in [8]. Until the advent of Free Electron Lasers (FEL), with their combined ultra-short pulse duration (tens of femtoseconds) and high intensities, X-ray pulse duration mainly allowed for the study of states where electronic and ionic temperatures were already the same. Now, this emerging technology has renewed interest in the non-equilibrium properties of WDM states [9–11].

―――――

*Electronic address: sebastiao.antunes@tecnico.ulisboa.pt

FELs are, however, limited in access and beam time due to high construction and operational costs.

Optical lasers also present an opportunity to create WDM states in non-equilibrium setups, but only in the skin-depth layer, with a typical scale of tens of nm, for metals [12]. The method is also constrained by the expansion times of the foil. This approach has the distinct advantage of being widely accessible when compared to FEL isochoric heating experiments, while still allowing access to non-equilibrium states of WDM. Both FELs and optical pumps are plagued by the creation of transverse temperature gradients by the spatial shape of the energy source. Typically, the longitudinal gradients can be reduced, if thin enough foils are chosen.

Time-resolved diagnostics of appropriate time resolution are necessary to study the properties of the transient warm dense states. Otherwise, a measurement with a single time stamp can be contaminated by widely different temperatures, pressures, and densities, as these quantities vary over time. The study of conditions before a thermal electronic distribution is established is only possible with sub-picosecond resolution techniques, which are then deployed to study fast equilibration dynamics and subsequent processes.

X-ray absorption experiments, when close to absorption edges (XANES: X-ray Absorption Near Edge Spectroscopy) provide direct information about both the valence electrons and the short-range atomic order [12]. For the diagnostics to work, however, it needs broadband high-brightness radiation on a time scale compatible with the desired time resolution. On the side of large facilities, while synchrotrons provide the necessary broadband radiation their pulse width of $\tau_p \approx 100$ ps severely limits temporal resolution and consequently the ability to perform IH non-equilibrium studies. [4]. The tabletop versions of such experiments are constrained in their time resolution by the availability of broadband X-ray sources of small enough duration (they are typically produced from plasma emission inherently limited due to heating and cooling dynamics of the plasma [12] but can also be sourced from Betatrons). Source intensity is also a limiting factor as it regulates the number of shots needed for obtaining a spectrum. In WDM conditions, the sample is expected to ablate, creating a bottleneck in said acquisitions, since there is a need to move or replace the sample after each shot.

In this article, our focus will be on the transient, warm dense, non-equilibrium states created by heating of thin Titanium films, with femtosecond near-infrared (NIR) laser pulses. We will directly probe the electronic structure by exciting bound-free transitions using extreme ultra-violet (XUV) radiation to image the solid-density plasma. Due to the ultra-fast nature of our pump and probe, a ~ 50 fs time resolution was achieved, allowing the study of non-equilibrium electronic properties and separation of electronic and ionic effects. The spatial resolution of our setup, on the other hand, turns the transverse spatial gradients created by the pump's spatial shape into a strength, by multiplying the number of data points obtained per shot, one for each different sampled condition. Furthermore, several data series were acquired for different total pump energies. The respectable amount of data obtained will then justify the Bayesian Inference approach taken to estimate parameters and uncertainty.

2. EXPERIMENT AND DATA

2.1. Experimental Setup

Our pump consisted of a NIR pulse, intensities up to $I \approx 10^{14}$ W/cm^2 ($F \approx 5 \times 10^4$ J/m^2). The absorption of 800 nm light in titanium, at our laser intensities, is dominated by inverse bremsstrahlung (IB), making intra-band absorption the dominant process. Direct absorption by phonons does not play a significant role as the pulse duration is much shorter than their period. Ionization effects are also small within the temperature ranges studied here.

The intensity of the pulse decays exponentially, within the sample according to:

$$Q_{abs}(x,r,t) = \frac{2}{\delta_s} AI(t,r) \exp(-2x/\delta_s). \qquad (2)$$

where $A = 1 - R$ with $R = 0.558 \pm 0.001$ the Fresnel reflection coefficient at a boundary measured experimentally, and δ_s is the skin-depth, the characteristic length over with the intensity of the field decays to $1/e$ of its initial value.

A schematic representation of the experimental setup is shown in figure 2. A Near-Infrared femtosecond laser with wavelength $\lambda_l = 800$ nm, pulse duration $\tau_l = 50$ fs, a spot size of $W_l = (90 - 140)$ μm and a Gaussian spatial profile was used. The initial beam was split using a polarizing beam splitter into a pump (marked IR in figure 2) and a probe pulse (marked XUV).
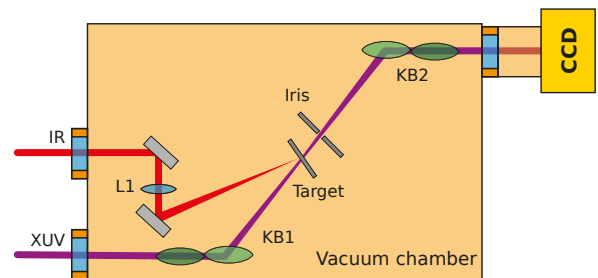

FIG. 2: The experimental setup

The pump pulse's total energy was varied between 50 μJ and 1 mJ, which represents a range of laser intensities $I_{pp} \approx (10^{13} - 2.5 \cdot 10^{14})$ W·cm^{-2}. The probe pulse was focused onto a gas cell to create an XUV spectrum through High Harmonic Generation (HHG) [13]. After the HHG gas cell, filters remove any remaining NIR and we are left with an ultrashort XUV pulse.

The HHG process created a low intensity pulse with fluence $F_{pb} = 5$ nJ/cm^2 and pulse duration $t_{pb} = 25$ fs corresponding to an intensity $I_{pb} = 2 \cdot 10^5$ W/cm^2. As such, this pulse needed to be kept in primary vacuum so that it would not be attenuated by air. The generated spectrum was measured at the exit of KB2, through a slit and gradient combination. Taking into account the several harmonics present, the weighted average of the probe is 26.2 eV.

Both the pump and the probe pulses were focused onto a thin (100 nm) Ti film, with Kirkpatrick–Baez (KB) mirrors being used for the probe pulse. The spatial imprint of the radiation transmitted through the film was recorded by a CCD with an Al filter that only allows radiation in the (17-80) nm or, approximately, (15.5-73) eV range.

Using a translation stage, the optical path of the probe pulse was altered and, thus, the time delay between the arrival of the pump and the probe was indirectly varied. This allowed for the collection of temporal data series composed of several transmitted XUV spatial imprints.

The temporal resolution of the collected data was at best 50 fs due to the probe pulse's duration while the spatial resolution is constrained by the overall resolution of the system: each pixel of the final image translates to (7×7) μm^2 of the foil.

At the pump intensity range achieved by this setup, the metal ablates away some time after the initial excitation. As such, after each shot, the target's position needed to be changed so that a new portion of the film was irradiated. The shot-by-shot nature of the experiment was the main limitation in terms of the number of data points that could be measured.

2.2. Acquired Data

For each of the translation stage's position (representing a time delay between the arrival of the pump and the probe to the Ti film) and each of the pump pulse's total energy chosen values (50, 150, 250, 500, 1000) μJ, three different types of images of the transmitted XUV radiation were recorded.

First, an image of just the XUV pulse was taken, shown in figure 3a; immediately after, and because the metal did not ablate, both pulses were sent in and a second image was taken - figure 3b. A final shot was acquired, with the pump switched off, as exemplified in figure 3c. This last one was designed to image the ablated portion of the metal film, due to the pump sent in the previous shot.

The grid that can be seen in all the acquisitions are images of the support bars for the metal film. The area of each square is (360×360) μm^2. It is not orthogonal due to optical aberrations, namely astigmatism caused by the grazing optics nature of the KB mirrors utilized. The acquired images can have both positive or negative time stamps. It is positive if the pump arrived before the probe, and vice-versa.

the XUV transmission spectrum of Ti was also acquired and compared to the HHG spectrum,

2.3. Analysis

The acquired XUV-transmission images had to be corrected for spatial background effects of the CCD; zoomed in to get rid of artifacts like other bright spots in the film, caused by tears or previous holes; and for plasma self-emission - when in the XUV range. This last effect plagues mostly the highest fluence zones but the correction was performed on all data sets, with adjusted magnitude, for consistency.

To properly define the zone of interest (where the sample was significantly disturbed) we then turned to figure 4a (a background-corrected zoomed-in version of 3c). The ablated area could be defined as the zones where the CCD counts are significantly higher, i.e. where the XUV pulse of the $t = \infty$ acquisition, is not attenuated by the Ti film. To obtain matrices, or masks, like the ones shown in figure 4b (ones inside the zone of interest and zeros outside) a threshold method was applied.

To take advantage of the spatial resolution the ablated region had to be subdivided into several sub-zones, in which the XUV transmission will be averaged, to reduce the noise levels. The main hurdle of subdividing the zone of interest was related to the fact that, from image to image, even in the same time series, the depression in transmission moves from place to place and it also moves relative to the geometric center of the defined area of interest. To accurately track the center of the depression, a new 2-dimensional least-squares regression was performed, using [14], for each acquired data point in all the different time series. The lower energy series were fitted to a 2-dimensional Gaussian and the higher energy time series were fitted to a self-made function since the shape of the depression was observed to be changing from a connected shape to a "ring" one.

Figures 5a and 5b show representative results of this least-squares fit, where good agreement was found between the zoomed-in and corrected data and the reproduction based on the fit process described before.

With the center coordinates of the depression uniquely determined for all temporal times stamps, in each data series, circular and concentric subdivisions of the zone of interest could be drawn. These inner zones' radii were calculated as a fraction of the radii of the zone of interest. As such, the radii of the sub-zones vary from image to image, in the same series, just as the radius of the overall zone of interest. These variations, however, are not more than one to two pixels inside the same temporal data series, while being considerably larger for different series. The fraction of the total radii used was manually adjusted, between different series, to guarantee that the area of the sub-zones did not differ too much, which was important for a statistical experimental error determination. In figure 5c an example of the resulting subdivisions can be seen.

With the zone of interest properly located and subdivided and with the $S_{pp,E}$ and $S_{pb,E}$ matrices corrected for the different spatial background effects (here the subscript E refers to the total energy of the pump pulse used in the corresponding data series), the calculation of the relative transmission for each zone could be tackled. This was done by straightforwardly by:

$$T_E(z,t) = \sum_{(i,j) \in z} S^{pp,E}_{ij}(t) \Big/ \sum_{(i,j) \in z} S^{pb,E}_{ij}(t) \qquad (3)$$

where $T_E(z,t)$ represents the relative (to the probe only image) XUV transmission of zone z, indexed by its temporal series' pump energy E and relative position of the sub-zone being calculated ($z = \{inner, middle, outer\}$), at a time delay between the pump and the probe t. The sum was performed pixel by pixel, subject to the restriction that they belong to the appropriate sub-zone.

The tagging of the series with the total pump energy and spatial position of the sub-zone is, however, not useful, since these taggs do not properly encapsulate the physical information needed for a forward model to simulate our data sets. As such, the average absorbed fluence on each sub-zones was calculated by reconstruction of the spatial profile of the laser and knowledge about the ablation threshold.

As the measurements were taken a few days apart, the waist of the laser possibly changed from series to series. Changes in the aperture of the pump beam also contributed to this effect. To quantify such changes an
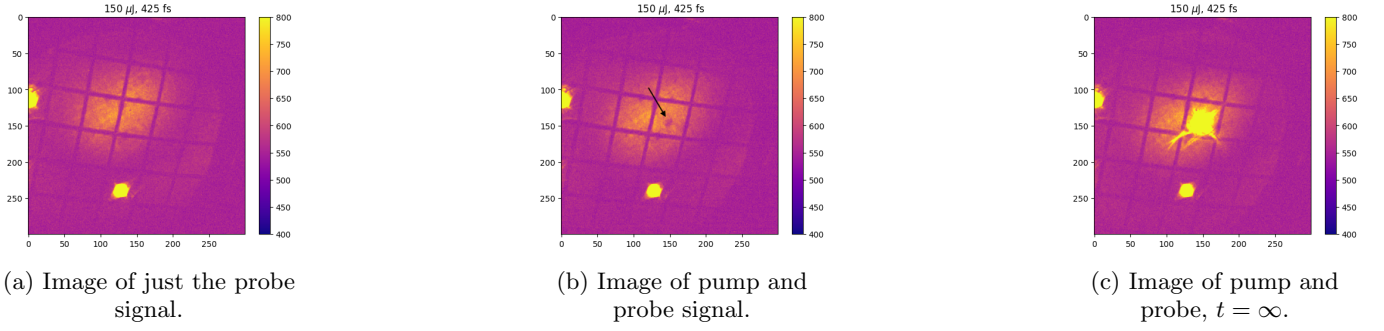
(a) Image of just the probe signal.

(b) Image of pump and probe signal.

(c) Image of pump and probe, $t = \infty$.

FIG. 3: Images of the transmitted UV radiation, for 150 μJ pulse energy and 425 fs of delay.

(a) Shot at $t = \infty$.

(b) XUV only shot.

FIG. 4: 40×40 zoom in of a 500μJ shot, at 200 fs.

(a) Corrected area of interest.

(b) 2D Gaussian fit to 5a.

(c) Desired division of the zone of interest.
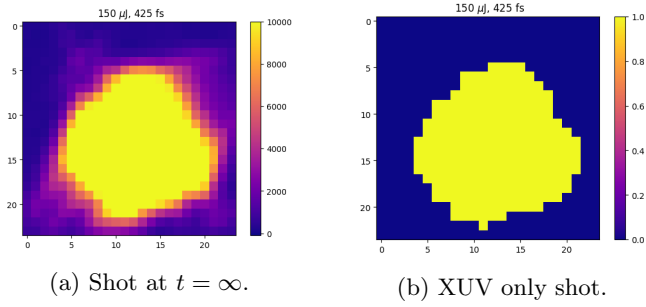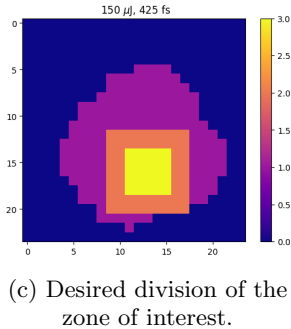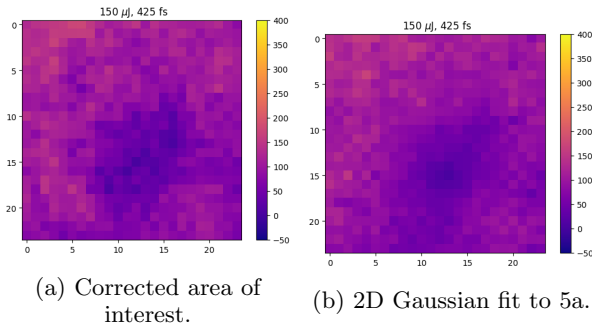
FIG. 5: Subdividing zone of interest, 150 μJ series at t=425 fs.

inverse problem was solved consisting of determining the waist, w, of the pump laser pulse, assumed Gaussian, that would create an ablated zone equal in area to the average area of the zone of interest, of a given series, knowing the ablation threshold, reported in [15] to be $F_{th} = (74 \pm 13)$ mJ/cm^2. The knowledge of the laser's spatial profile directly translates to the profile of the absorbed laser fluence.

In figure 6, the obtained temporal fluence-tagged data series are shown. The series with similar average absorbed fluence were grouped for better understanding, as

in total there are 21 different temporal series, each referring to a different sub-zone, i.e. a different fluence and final state.
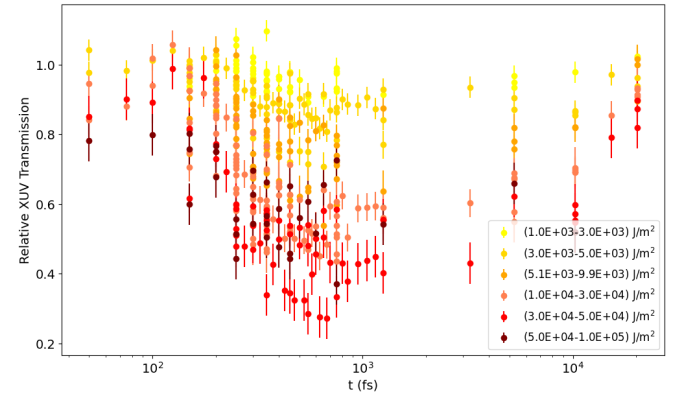

FIG. 6: Relative (to probe only) transmission, as a function of time, grouped by absorbed fluence of the sub-zone of each series. Laser pulse peaks at 250 fs. Log scale.

In the plot, the initial drop in the XUV transmission coefficient can be seen approximately at the same time as the laser is peaking (t=250 fs), with a possible small delay relative to the pump pulse, i.e. to positive times. This was interpreted as the fast electronic response to the laser pulse of the electrons in the skin depth of the material. In general, it can be concluded that the higher the absorbed fluence, the higher the XUV opacity (lower transmission coefficient), with the notable exception of the higher fluence group, exemplifying the "ring" effect. After the (200-300) fs mark there is stabilization and even a slight recovery of the transmission.

The picosecond response can also be observed, with all the data collected plotted, i.e. up to t=20 ps, depending on the series. Given it takes picoseconds to be noticeable, this trend is necessarily ionic, since the probe pulse was XUV and, thus, only sensitive to changes in the electronic distribution. This response can be identified with the release of thermal energy from the electronic to ionic population. In this regime, the XUV transmission coefficient can be seen to recover along a similar time scale for all the fluence groups, with its value approaching the cold measurements in all cases.

3. THEORY AND MODELS

3.1. TTM

The electron-ion (e-i) equilibration taking place after sample excitation can be described by a simplified version of the Two-Temperature model (TTM)[16]. This model has the distinct advantage of computational simplicity and has been amply shown to describe the pre-ablation moments of a thin irradiated metal sample after the electronic population is in equilibrium, within itself, and can be said to have a temperature.

Note that, since we are interested in the first few ps after irradiation of a thin film, thermal dissipation effects will be neglected in the TTM. Changes in the electronic density will also be disregarded, as there is little to no ionization of core electrons expected at our irradiation intensities. The model's master equations are:

$$
C_e\left(T_e\right) \frac{\partial T_e}{\partial t} = S_{abs}(\boldsymbol{r}, t) - G_{ei}\left(T_e\right)\left(T_e - T_i\right) \text{ and}
$$
$$
C_i \frac{\partial T_i}{\partial t} = G_{ei}\left(T_e\right)\left(T_e - T_i\right) \tag{4}
$$

$S_{abs}(\boldsymbol{r}, t)$ is the absorbed laser power density and $G(T_e)$ is the electron-phonon/ion coupling factor. This last factor needs to be calculated from physical considerations and several models have been proposed for it [17–22].

In [17], the heat capacities of electron populations with finite temperatures in cold metal latices as well as the e-i coupling coefficient were determined. The authors considered the electronic energy distribution as well as the density of states (DOS) of the different metals. No deviations from the cold DOS due to electron heating were considered, however. The electronic heat capacity was calculated from the definition, i.e, the derivative of total electron energy with respect to T_e, as such:

$$
C_e\left(T_e\right) = \int_{-\infty}^{+\infty} \frac{\partial f\left(\epsilon, \mu, T_e\right)}{\partial T_e} D(\epsilon) \epsilon d\epsilon \tag{5}
$$

where $D(\epsilon)$ is the DOS that the authors calculated for cold metals, using ab initio DFT simulations and assumed constant for different electronic temperatures, and $f\left(\epsilon, \mu, T_e\right)$ the electronic distribution function (in this case a Fermi-Dirac).

The parameter $G(T_e)$ of the results we will present here will be considered constant in time, and as such over a range of temperatures. We will use parameter estimation techniques to try and adjust a different G_{ei} to each sub-zone being considered. When the same estimation algorithm was performed on joint searches over all sub-zones, with $G_{ei}(T_e)$ calculated as in equation 5 the overall performance of the fit dropped slightly, and, so, the more data-driven and less a priori constrained searched was preferred.

Since the ablated region (roughly the size of the laser pulse) was divided into three regions of interest, it was assumed that, within each region, the laser intensity does not vary spatially. That is, a single average fluence (corresponding to the same total absorbed energy per zone, as with the Gaussian distribution) is considered for each of the zones. The source term expression is then written as:

$$
S_{abs}(t) = \frac{AI(t)}{\delta_s}, \text{ with}
$$
$$
I(t) = \sqrt{\frac{4\ln(2)}{\pi}} \frac{FA}{\tau_p} \exp\left\{-4\ln(2)\left[\frac{(t - t_0)}{\tau_p}\right]^2\right\} \tag{6}
$$

with F being the average incident fluence of a given zone of interest and $A = 1 - R$ with R the reflectivity coefficient, measured to be $R = 0.558 \pm 0.001$.

Finally, with all the terms in equation 4 properly defined ($C_i \approx 3/2k_B$), a computational algorithm can be deployed to solve it for the time evolution of the distribution function. Note that, since an equilibrium electronic distribution is assumed and the model only evolves temperature, the chemical potential μ has to be determined separately. This can be accomplished by the requirement of particle number conservation - $n_e = \int f(\varepsilon, \mu, T_e) \cdot D(\varepsilon) d\varepsilon$ - consistent with the fact that no ionization of core electrons is expected.

In the simulations presented below the DOS function was considered nearly free since the cold Ti DOS provided poor agreement with the acquired data series, even after model optimization. In this framework, the electronic mass is allowed to take an effective value, but otherwise, the dispersion relation remains that of a free electron, such that the DOS takes the form:

$$
D(\varepsilon, m_{eff}) = \frac{\sqrt{2 \cdot \varepsilon \cdot m_{eff}} \cdot m_{eff}}{\pi^2 \hbar^3}. \tag{7}
$$

3.2. Quantum Boltzmann model

In [18], a much-used Boltzmann equation model for thin metal sheets being irradiated by femtosecond IR and optical laser light was developed. This type of model offers the opportunity to study non-thermal electron-electron (e-e) effects since it does not assume instantaneous thermalization of the electron gas to a Fermi-Dirac distribution. Due to the high degree of computational complexity of the Boltzmann equation, several simplifying assumptions were laid out first.

Firstly, the material is assumed homogeneous and isotropic. This is justified by the fact that the metal sheet is composed of micro-crystals oriented differently from one another and it allows us to take an average of all polarization directions of the incident laser light. Furthermore, spatial variations of the intensity of the laser pulse, as it is being absorbed transversely, can be neglected, for films with thickness on the order of the absorption depth of the metal. Other transverse spatial effects, such as diffusion and energy transport were also neglected. This last assumption is consistent with a thin layer approximation and a focus on time-dependent effects such as energy absorption and thermalization amongst the electrons (first) and of electrons with the lattice (latter).

Taken together, these impositions make the distribution function only dependent on time and energy and, as such, reduce the electronic Boltzmann equation to:

$$
\frac{\partial f(k)}{\partial t} = \left.\frac{\partial f(k)}{\partial t}\right|_{\text{e--e}} + \left.\frac{\partial f(k)}{\partial t}\right|_{\text{e--i--pt}}. \tag{8}
$$

The dynamics of the systems are then encapsulated in collision terms, caused by different microscopic processes. The relevant terms refer e-e and e-i-pt (electron-ion-photon) collisions. The electron-phonon collision term will not be considered here, since our goal is model possible laser-induced non-equilibrium effects of our electron gas. These are expected to take place over hundreds of femtoseconds (shorter than e-i/phonon timescales) if long-lived thermal electrons were to be observed [10]. As was previously discussed, the main process for deposition of energy, at these fluences and wavelengths is IB, i.e. e-i/electron-phonon collisions that allow for momentum conservation while absorbing one or multiple photons. We will only consider elastic collisions here (amounting to classical, infinitely massive ions), using the same arguments laid out for the electron-phonon collision term.

Two detailed collision terms need to be determined. The e-e one concerns a two-to-two scattering event and the e-i-pt one concerning a two-to-one event since the photon is absorbed and the ion's momentum does not change. These collision sums/integrals have standard forms, given in [7], that depend on the scattering probability per unit time and on Pauli blocking factors. The former can be calculated from the fermi Golden Rule with perturbation theory if the interaction potential is weakly time-dependent [7]. Rethfeld et al [18] propose that a statically screened Coulomb potential be used to model this potential and also a single parabolic conduction band the dispersion relation of the free electrons is given by $\epsilon(\boldsymbol{k}) = \hbar^2 k^2/2m_e$. They thus write:

$$
\left.\frac{\partial f(\boldsymbol{k})}{\partial t}\right|_{\text{el}-\text{el}} = \frac{2\pi}{\hbar} \sum_{\boldsymbol{k}_1} \sum_{\boldsymbol{k}_3} \left(\frac{e^2}{\varepsilon_0 \Omega} \frac{1}{\Delta k^2 + \kappa^2}\right)^2
$$
$$
[f_{\boldsymbol{k}_3} f_{\boldsymbol{k}_1}(1 - f_{\boldsymbol{k}})(1 - f_{\boldsymbol{k}_2}) - f_{\boldsymbol{k}} f_{\boldsymbol{k}_2}(1 - f_{\boldsymbol{k}_3})(1 - f_{\boldsymbol{k}_1})]
$$
$$
\delta\left(\epsilon_{\boldsymbol{k}_3} + \epsilon_{\boldsymbol{k}_1} - \epsilon_{\boldsymbol{k}_2} - \epsilon_{\boldsymbol{k}})\right)
$$
$$(9)$$

where $\Delta\boldsymbol{k} = \boldsymbol{k}_1 - \boldsymbol{k}_2 = \boldsymbol{k} - \boldsymbol{k}_3$ is the exchanged momentum and $\boldsymbol{k}_2 = \boldsymbol{k}_1 - \boldsymbol{k} + \boldsymbol{k}_3$ to ensure conservation of momentum. The Fourier Transform operation performed on the screened Coulomb potential leads to the appearance of a volume term Ω, corresponding to the total volume of the crystal being modeled, but is inconsequential as it cancels out further along when the sums are transformed to integrals. The inverse screening radius can be obtained from the Vlasov equation, as discussed with equation 1. With the free dispersion relation being assumed, the expression can be written as [7], [18]:

$$
\kappa^2 = \frac{e^2 m_e}{\pi^2 \hbar^2 \epsilon_0} \int_0^\infty f(k) dk. \tag{10}
$$

As for the absorption term, the aim is to accurately model the IB process, in a microscopic and kinetic fashion. As derived in [23] and used in [18], the probability of absorption of n photons by an atom can be calculated by the time-dependent Schrödinger for free electrons disturbed by classical E-M radiation (the quantum nature of the photons can be disregarded as there is a great many of them in a given energy state). Afterward, first-order perturbation theory was applied to calculate the desired transition probability (taking the nucleus potential as the perturbation). The absorption (e-i-pt) term for the Boltzmann equation can then be written as:

$$
\left.\frac{\partial f(\boldsymbol{k})}{\partial t}\right|_{\text{el}-\text{ion}-\text{phot}} = \frac{2\pi}{\hbar} \sum_{\Delta\boldsymbol{k}} \left(\frac{e^2}{\varepsilon_0 \Omega} \frac{1}{\Delta k^2 + \kappa^2}\right)^2
$$
$$
\sum_{\ell=-\infty}^{\infty} J_\ell^2 \left(\frac{e\boldsymbol{E_L} \cdot \Delta\boldsymbol{k}}{m_e w_L^2}\right) \delta\left(\epsilon_{\boldsymbol{k}+\Delta\boldsymbol{k}} - \epsilon_{\boldsymbol{k}} + \ell\hbar\omega_L\right)
$$
$$
[[f_{|k+\Delta k|}(1 - f_k) - f_k(1 - f_{|k+\Delta k|})]]
$$
$$(11)$$

where in this case Ω will not cancel out, since there is a single sum that will be transformed to an integral, and can be identified with the volume of the unit cell Ω_0.

By switching the sums here presented into integrals, with the usual method, to integrals and analytically simplifying them we could deploy computational calculations to solve the Boltzmann equation 8. The electron-ion-photon collision term as written in equation 11 requires the electric field inside the material, as an input parameter. To calculate it, the average incident fluence of each sub-zone was converted to intensity through equation 6 and subsequently the formula $E_L(t) = \sqrt{2I(t)/(c\varepsilon_0)}$ was applied. 25 orders of the Bessel function had to be considered, due to our high electric field intensity, in the skin depth of the sample.

3.3. The observable

A schematic representation of the pumping and probing process, complete with the electronic distributions and the cold DOS of Ti, is present in figure 7. The only allowed transitions, at the probe pulse's average energy are the $3p \rightarrow$ continuum ones. Since the probe is of low intensity, linear response theory applies, and $\sigma_{\mathbf{k}} \propto (1 - f(\varepsilon_{\mathbf{k}}))$. As such, the variation in time of the absorption of the probe is, to first order, dependent on the distribution function of the pumped continuum electrons.
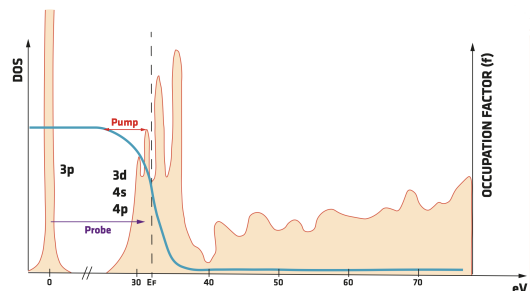

FIG. 7: A schematic representation of the pumping and probing process complete with the electronic distributions and the cold DOS of Ti.

Given that the $3p$ core states are very localized in energy, the pump will induce electronic transitions to the continuum with an energy distribution in the shape of the HHG spectrum. This happens because the number of XUV-excited electrons that transition to the continuum is proportional to the intensity of the radiation, at a frequency matching the energy gain of those electrons. The transitions will only be allowed if there are free continuum state for the core electrons to occupy, according to the Pauli exclusion principle.

The energy levels the XUV-excited electrons will try to occupy in the continuum are difficult to pinpoint since the absolute energy difference between the core state $3p$ and the beginning of the continuum (or, more practically,

between the core state and the Fermi energy) is itself hard to estimate, in a DFT framework. This will be one of teh adjustable model parmeters.

To obtain the relative to cold XUV transmission time series from the knowledge of the electronic distribution function it can be stated that:

$$T(f, \varepsilon_t) \propto 1 - \frac{\int (1 - f(\varepsilon, t)) \cdot HHG(\varepsilon_t)}{\int HHG(\varepsilon, \varepsilon_t) d\varepsilon} d\varepsilon \qquad (12)$$

with T being the transmission coefficient (both averaged in energy over all the XUV spectrum), and $HHG(\varepsilon, \varepsilon_t)$ being the XUV-excited electronic distribution, in the shape of the HHG spectrum. The ε_t model parameter defines the position of this spectrum in the energy scale of the continuum electrons. It is the distance, in energy, between the highest harmonic peak and the Fermi energy such that for negative values the spectrum is, on average, below this energy. For the forward model simulation run henceforth this ε_t parameter will be allowed to vary in the range $[-10, -4]$ eV. This acts as a prior since we know all harmonic peaks must be below the Fermi level. Note that a typical Fermi level of around 10 eV is expected.

Figure 8 shows the integrand of equation 12, plotted against energy, with the zero energy level being the beginning of the continuum states, along with $1-f$ for f the Fermi-Dirac distribution and an XUV-excited electronic spectrum, for a given ε_t. From figure 8a to 8b, energy has been deposited in the electronic distribution and so the Fermi level tilted in energy. Since most of the harmonic spectrum was below that level, this tilting contributes to an opening of vacancies for transitions, observable in the increase in the area below the total integrand function. This will translate into increased absorption and decreased transmission.
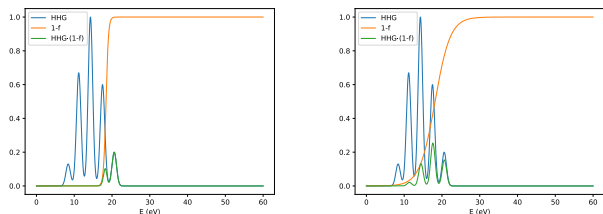
(a) Plot for $(1 - f)$ calculated at the beginning of the simulation, for cold Ti.

(b) Plot for $(1 - f)$ calculated 150 fs after the peak laser energy was deposited.

FIG. 8: Integrand of equation 12, as a function of energy and its two components for $\varepsilon_t = 4$ eV. $(1 - f)$ was calculated from a TTM simulation.

4. RESULTS AND DISCUSSION

The physical model presented allows us, to simulate, for the different data series acquired, the relative to cold XUV transmission, as a function of time. The TTM will be used for the 20 ps (after pump excitation) over which the series were acquired, and the Bolztamn model will be applied over the first 400 fs, long enough to determine whether non-thermal effects play a role, for our xperimental conditions.

Given the amount of data obtained and the probable difficulty in the fitting process, arising from multiple lo-

cal minima and regions of high correlation between different input parameters, we took a Bayesian Inference approach to estimate the models' parameters and their uncertainties. For each model, either joint searches, over all sub-zones, or independent searches for each of them were conducted. We show here only some of those results.

The searches themselves are a two-step process. First, a likelihood function (constructed from the forward model and data series) is optimized, using the Covariance Matrix Adaptation - Evolution Search algorithm [24]. This algorithm is robust to inversion instabilities and high correlation regions present in the function being optimized. Second, affine invariant Markov Chains Monte Carlos [25] are launched to explore the parameter space, around the global minima. This will sample how experimental uncertainty (also included in the likelihood function) affects the estimation of our input parameters and uncover correlations between them.

4.1. Multivariate analysis using the TTM

In order to provide more parametric freedom to the G_{ei} and m_{eff} coefficients especially, an independent MCMC search was run for each of the sub-zones, instead of relaying in a theoretical calculation. As a result, a different set of marginalized posteriors and 2D correlations was obtained for each of the sub-zones of interest studied, namely all the 150 μJ series and the two innermost zones of the third family of series with 250 μJ, each represented by a different color in 9 and 10.
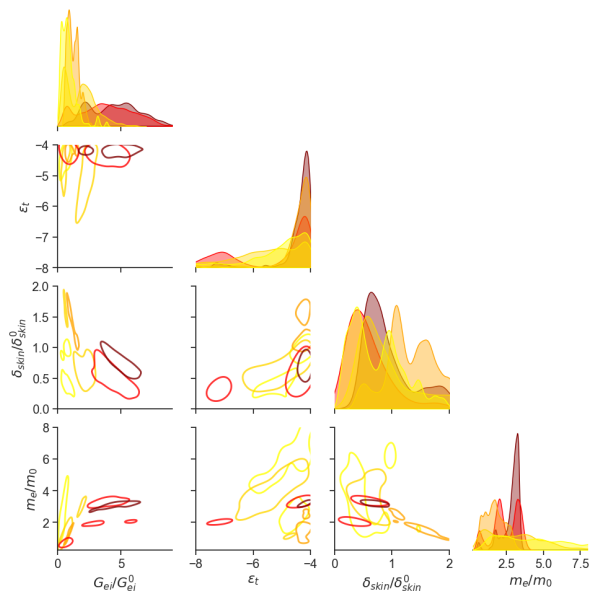

FIG. 9: 2D correlations and marginalized posterior distributions of MCMC searches performed for a physical forward model of a TTM, with constant G_{ei} and DOS as in equation 7. Ensemble of 40 walkers. The darker line on the 2D correlation is the 1σ band.

For these MCMC searches, the G_{ei} coefficient was considered constant, during a given time series, with its value being one of the free parameters. Nonetheless, a nearly free electron DOS approximation was deployed to calculate C_e. In table I, the central estimations and 1σ error bars are shown, for all sub-zones and inputs of the physical forward model. Combining these two pieces of information, agreement between the searches can be found

for the parameters δ_s and ε_t. Looking at the 1σ intervals, they appear broadly compatible with one another and the posterior distribution of these two parameters have overlaying highest probability regions. Physically, this was expected to be the case since neither skin-depth nor core-to-continuum state energy differences are expected to be dependent on laser intensity. Their constancy through the different MCMC searches is then a sanity check for the convergence of the algorithm and an indication of the robustness of the estimation of such parameters.

F (J/m²)	G_{ei}/G_{ei}^0	ε_t(eV)	δ_s/δ_s^0	m_{eff}/m_{eff}^0
0.3×10^4	$0.74^{+0.56}_{-0.41}$	$-4.85^{+0.68}_{-2.04}$	$0.67^{+0.53}_{-0.38}$	$4.16^{+3.22}_{-2.32}$
1.4×10^4	$1.17^{+0.55}_{-0.39}$	$-4.28^{+0.2}_{-0.43}$	$1.38^{+0.47}_{-0.42}$	$1.66^{+0.82}_{-0.66}$
4.2×10^4	$4.53^{+2.15}_{-2.29}$	$-4.23^{+0.16}_{-0.36}$	$0.80^{+0.76}_{-0.26}$	$3.04^{+0.25}_{-0.67}$
0.9×10^4	$1.69^{+1.02}_{-1.08}$	$-5.47^{+1.14}_{-2.11}$	$0.83^{+1.14}_{-0.34}$	$2.62^{+2.19}_{-1.40}$
2.3×10^4	$3.86^{+2.45}_{-2.25}$	$-4.78^{+0.65}_{-2.71}$	$0.52^{+0.95}_{-0.28}$	$2.26^{+1.98}_{-0.60}$

TABLE I: Most likely value and 1σ errors of the 5 MCMC searches performed, one for each sub-zone, for a physical forward model of a TTM, with a constant coupling parameter and nearly free electron DOS. F is the incident fluence in a given sub-zone

Considering the G_{ei} and m_{eff} posteriors and estimates, they appear to change more from zone to zone (or incident fluence). This behavior is expected of G_{ei} since it depends on T_e, intimately linked with the absorbed fluence of a given sub-zone. The m_{eff} dependency on electronic temperature is subtler in nature and comes from the fact that different deposited energies excite continuum electrons into different parts of the Ti DOS. Looking at figure 7 it is clear that lower excitation energies that do not dislocate the electrons from the d-band have a higher effective mass than the hotter ones that are excited into the $4s$ band. These theoretical considerations are only partially confirmed by the results from the MCMC searches, with the notable outlier being the 150 μJ inner zones, with higher than expected m_{eff}. These deviations from expectation might be the result of the increased parametric freedom of the forward model, with important correlations between the input parameters expected (such as m_{eff}, a proxy for C_e, vs δ_s, controlling the absorbed power density).

Looking at the 2-dimensional correlations of figure, we shall focus first on the ones involving the skin depth, as this is the parameter that directly controls the power density absorbed by a given sub-zone of interest (the average fluence and τ_p are fixed). The energy density deposited in the Ti film determines, in turn, the physical regime we are dealing with.

First, it is important to note that since the simplified TTM employed disregards the transverse absorbed energy gradient, because it is strongly attenuated in a few ps and our experimental observable is not sensitive to it, a longer skin depth is associated with a lower energy density for a given sub-zone. This is due to the fact that the volume over which the same fluence is attenuated/absorbed is bigger. From here the direct correlation between ε_t and δ_s becomes apparent: the further the HHG spectrum is from ε_F then, to achieved the same

$\min(T_r(\varepsilon_t, t))$ - our observable -, the higher T_e needs to reach. Since a higher T_e, all else being equal, requires more energy density - that is a smaller skin depth - the direct correlation between the parameters is then explained.

The inverse correlation between δ_s and m_{eff} can be explained similarly: heavier electrons take more energy to achieve a given T_e than lighter ones. As such the higher the electronic mass, the higher the skin depth needs to be to achieve the same XUV transmission.

Regarding the δ_s versus G_{ei} correlation, an inverse correlation between the parameters is found. In this case, more deposited energy, in the form of a lower δ_s, leads to a higher e-e coupling. Having reached higher energy, to recover to the same final XUV transmission, in an amount of time determined by the experimental data, electrons need to exchange energy with the ions at a faster rate, explaining the correlation.

Finally, the inverse correlation between λ and ε_t also appears as strong and persistent between the two figures. It can be interpreted in a similar fashion to the other ones discussed: an HHG spectrum further away still requires higher T_e to achieve the same transmission. It also requires more rapid thermalizing when recovering to the same higher level again.

Figure 10 displays 100 forward model runs (for each sub-zone), selected independently from the MCMC-generated ensemble of walker chains after the burn-in period, plotted against each of the data of each sub-zone considered. The second and third-highest fluency zones display overlapping model predictions but also somewhat superimposed data points.

A good match was achieved between the experimental data and the forward model's 1σ band. Most data points, when considered with their uncertainty, fall within the band of results for their respective sub-zone. Other models run with a theoretically prescribed G_{ei} temperature dependence produced worse results in the region most sensitive to this parameter (the zone where the transmission recovers, i.e, in the picoseconds).
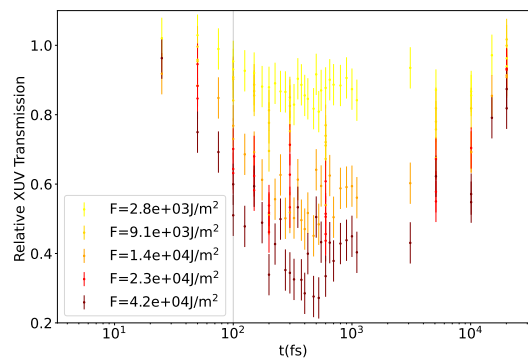

FIG. 10: 50 model runs with parameters sampled independently from the ensembles generated by the MCMC searches, for a physical forward model of a TTM, with constant G_{ei} and DOS as in equation 7, plotted on top of the experimental data. In log scale with the laser fluence peaking at 100 fs.

In figure 11, the central estimate and 1σ error bars for the G_{ei} parameter of each sub-zone considered is plotted. The estimates were calculated from the 100 model run, sampled form the MCMC-generated ensemble, for each sub-zone. Taken together however the results of all the sub-zones, plotted vs the maximum T_e achieved in a given

model run and sub-zone, allow us to devise G_{ei}'s temperature dependency. The results seem in agreement with FEG predictions for the three lowest fluency zones and a marked increase in coupling for the highest fluency zones. The overall tendency then is that of a sustained increase in G_{ei} with T_e, not predicted by any of the theoretical models considered.
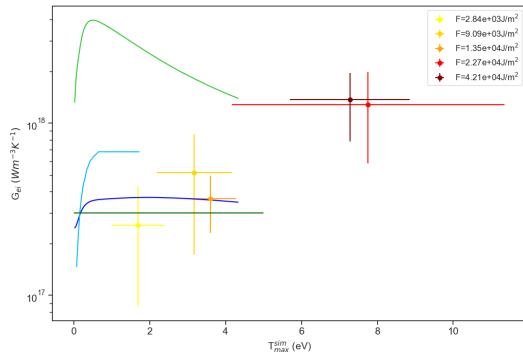

FIG. 11: G_{ei} vs maximum T_e, for each sub-zone considered. Sample comprised of 100 model runs, from MCMC search results for a forward model comprised of a TTM with constant G_{ei} and DOS as in equation 7. The light green line is the [17] result for a cold Ti DOS and the dark blue line refers to the same formula but an Al DOS. In dark green is the result of [18] for a FEG and in light blue the [22] predictions for Ti.

We plot the heat capacity central estimate and the 1σ bars of each sub-zone, with a similar method, in figure 12. The observable C_{ei} was not calculated from equation 5 but was approximated along simpler lines $C_e(T_e^{max}) \sim F/(T_e^{max} \cdot \ell_f)$, with $\ell_f = 100$ nm the thickness of the film and F the observed fluence of a given sub-zone. This was done so as to compare these C_e results with those from the Boltzmann model, and it provides a more cumulative estimation, over T_e, since the derivate is substituted for achieved temperature.
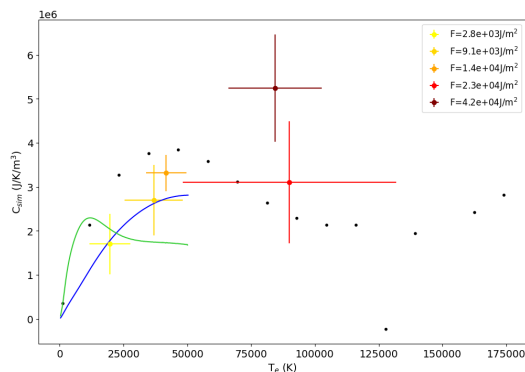

FIG. 12: C_e vs maximum T_e, for each sub-zone considered. Central estimate and error bars obtain by sampling 100 model runs, from MCMC search results for a forward model comprised of a TTM with constant G_{ei} and DOS as in equation 7. The light green line is the [17] result for a cold Ti DOS and the dark blue line refers to the same formula but an Al (or FEG-like) DOS. The black dots are the estimates from a finite temperature DFT simulation with a cold lattice, performed in the VASP package [26–30].

Since each sub-zone had its own effective mass, this parameter, also has a significant amount of freedom, effectively allowing it to draw its own peace-wise response,

in electronic temperature. The heat capacity parameter, despite this high parametric freedom, closely resembles Lin's Al prediction and the TD-DFT Ti results, with a notable outlier in the highest fluence sub-zone. Interestingly, this zone also exhibits a difference from the trend in terms of its effective mass. In both cases, the anomaly is positive which is expected since heavier electrons should take, in general, more energy to reach a given T_e.

4.2. Modelling electron relaxation using the Boltzmann model

Figure 13 displays the 2D correlation and marginalized posterior distributions of the Boltzmann model's free parameters. They were obtained from an MCMC search of the joint posterior distribution of all the sub-zones of the data family with 150 μ J. From the marginalized posteriors, we can extract the central estimates and 1σ error bar of or free parameters, as was done before, resulting in $\kappa_{ie} = 1.03^{+0.05}_{-0.05}$, $\kappa_{ee} = 1.25^{+0.47}_{-0.24}$, $m_{eff} = 1.61^{+0.29}_{-0.38}$ and $\varepsilon_t = -7.02^{+1.67}_{-1.44}$. The two screening parameters κ_{ie} and κ_{ee} are close to 1, the result expected for a quasi-free electron gas. The e-e screening coefficient, specifically, has a very small relative error but, even so, is compatible with $\kappa_{ie} = 1$. The effective mass estimate is above one, which is not unexpected given the strongly peaked d-orbitals at the beginning of the Ti continuum and near the Fermi energy (figure 7).
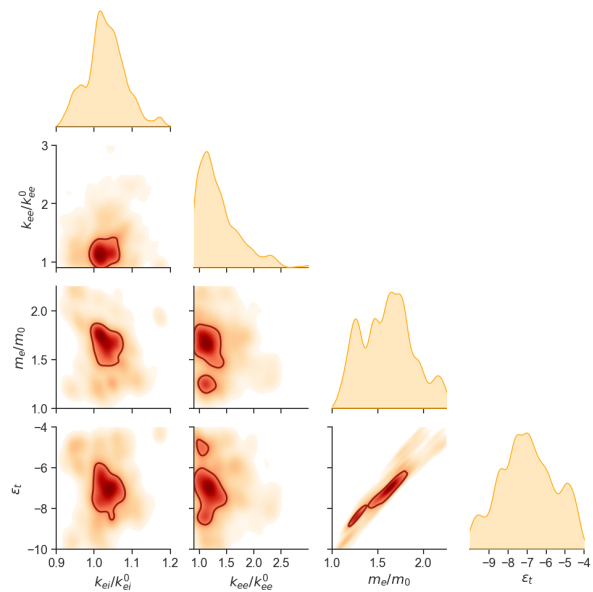

FIG. 13: 2D correlations and marginalized posterior distributions of an MCMC search performed for a physical forward model of the Boltzmann equation 8, without the phonon term. Family of 150 μJ data series utilized. Ensemble of 40 walkers, evolved for a total of 15000 model evaluations. 10000 evaluations discarded as burn-in. The darker line on the 2D correlation is the 1σ band.

Looking more closely at the 2D correlations of the posterior, only a strong direct correlation between the effective mass and ε_t stands out. All else being equal, a lower ε_t - corresponding to the HHG pulse exciting electrons to further away from the Fermi energy - requires a higher equivalent T_e to get the same amount of transmission drop. One of the ways of obtaining a higher equivalent T_e is, as discussed in the previous section, to reduce

the effective electronic mass thus reducing heat capacity. Interestingly, no similar correlation can be said to exist between the k_{ie} parameter and ε_t, as one might expect. From an algorithmic perspective, it remains unclear why this is the case since both parameters affect the equivalent T_e. The best hypothesis that the author can put forward is that the κ_{ie} parameter affects the different sub-zones differently, thus while one zone might be getting optimized with changes to κ_{ie} some other will fall out of agreement dramatically.
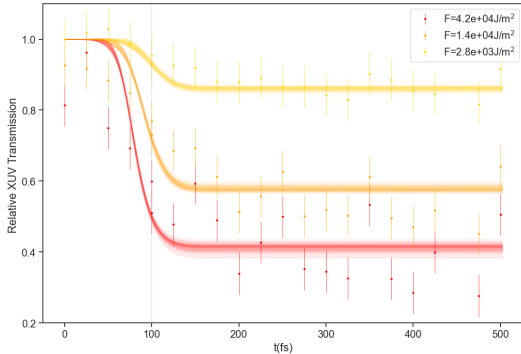

FIG. 14: 50 model runs with parameters sampled independently from the ensemble generated by the MCMC search, for a physical forward model of the Boltzmann equation 8, without the phonon term, plotted on top of the experimental data. In log scale with the laser fluence peaking at 100 fs.

Figure 14 plots the forward model results from fifty model runs, using fifty sets of parameters, independently chosen from the ensemble generated from the MCMC search, overlaying the obtained data series. Reasonable agreement is found between both in terms of the slope of the fall and of the level of stabilization of the transmission.

The fact that strong agreement is found for free electron-like parameters is notable. As discussed in the introduction, WDM is difficult to model due to the fact that it sits in a region where solid matter and plasma physics methods collide. Here, the results from a first principles model, seem to indicate only a slight material dependence of the model results (in the effective mass). For the experimental conditions of our sample, the electronic population behaves like a nearly-free, fast-thermalizing, electron gas. Both the closeness of the shape of fall in transmission to that of the TTM-modeled one; and observing the Boltzmann model runs, with the parameters set to their obtained central estimates, converging in tens of fs to a hot Fermi-Dirac distribution, validate the TTM assumptions of instantaneous thermalization of the electron gas, with itself.
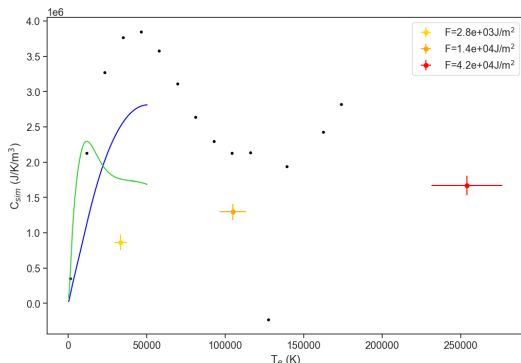

FIG. 15: C_e vs maximum T_e, for each sub-zone considered, calculated as for the TTM. Central estimate and error bars obtain by sampling 50 model runs, from MCMC search results for a physical forward model of the Boltzmann equation 8. The light green line is Lin's result ([17]) for a cold Ti DOS and the dark blue line refers to calculations with the same formula but an Al (or FEG-like) DOS. The black dots are the heat capacity estimates from a finite temperature DFT simulation with a cold lattice.

Figure 15 displays the estimate, performed as for the TTM, of the electronic heat capacity as a function of temperature. It has a shape congruent with a free-electron-like DOS (the blue line for Al), which was expected due to the nearly free DOS assumption of the model. The absolute value of the extracted heat capacity is, however, always significantly lower than the theoretical predictions.

5. CONCLUSIONS

Throughout this thesis, we presented a study of warm dense Ti, namely of its coupling parameters: both electron-electron and electron-ion. Using single-shot XUV imaging we could obtain three data sets, providing information on the behavior of continuum electrons, at different temperatures, simultaneously. The data gathered was paired with Bayesian Inference techniques to benchmark different models: ones tuned for ionic time scales, others to electronic ones.

We could conclude that e-e thermalization is quick, from the Boltzmann model, which validates the TTM assumption of instantaneous electron-electron equilibration, at our 50 fs time resolution. Correlations between the modeling parameters were found in the TTM runs, which show that a constant G_{ei} can be an effective assumption, in a large range of parameters, if such constant is adjusted for the incident pump intensity. A positive correlation was found between ε_t and δ_s/δ_s^0 while negative correlations prevail between δ_s/δ_s^0 and both G_{ei}/G_{ei}^0 and m_{eff}/m_{eff}^0. Overall a free electron gas and TTM can describe the data well. Values of G_{ei} were shown to increase with temperatures in the domain we probed, while being in the range of values previously published.

In terms of future work, both models would benefit from DFT Ti DOS calculations for elevated electronic and ionic temperatures. The Boltzmann model could be further expanded to include non-elastic e-i collisions and thus e-i energy exchange. Furthermore, different likelihood functions could be experimented with and Bayesian model selection could be attempted. On the experimental side, a measurement of ε_t is paramount for a reduction in the uncertainty over simulated T_e. Tighter control of the pump laser spatial profile and total energy would also contribute to results better tagged for average fluence. to better study non-equilibrium e-e effects, a shorter pump pulse would be required and an HHG centered closer to the Fermi energy.

The work here discussed was presented in poster formats on the 13th International Conference on High Energy Density Laboratory Astrophysics (HEDLA 2022) and at the Extreme Light Infrastructure (ELI) Summer School 2022 were it won the award for best scientific poster presentation. It was also accepted as an oral contribution to the Radiative Properties of Hot Dense Matter, at the Los Alamos National Laboratory.

References

[1] B. Xu and S. X. Hu, Phys. Rev. E **84**, 016408 (2011).

[2] R. P. Drake, L. Davison, and Y. Horie, *High-Energy-Density Physics: Fundamentals, Inertial Fusion, and Experimental Astrophysics* (2006), ISBN 978-3-540-29314-9.

[3] F. Graziani, M. Desjarlais, R. Redmer, and S. Trickey, *Frontiers and Challenges in Warm Dense Matter* (2014), ISBN 978-3-319-04911-3.

[4] K. Falk, High Power Laser Science and Engineering (2018), ISSN 20523289.

[5] K. Sugioka and H. Sun, Light: Science Applications **3**, e149 (2014).

[6] K. C. Engelhorn, Ph.D. thesis, University of California, Berkeley (2015).

[7] W. Ebeling, V. Fortov, and V. Filinov, *Quantum Statistics of Dense Gases and Nonideal Plasmas* (2017), ISBN 978-3-319-66636-5.

[8] D. HOoffmann, A. Blazevic, P. NI, O. ROosmej, M. Roth, N. Tahir, A. Tauschwitz, S. Udrea, D. Varentsov, K. Weyrich, et al., Laser and Particle Beams **23** (2005), ISSN 0263-0346.

[9] Bob Nagler et al, Nature Physics **5** (2009), ISSN 1745-2473.

[10] J.-W. Lee, M. Kim, G. Kang, S. M. Vinko, L. Bae, M. S. Cho, H.-K. Chung, M. Kim, S. Kwon, G. Lee, et al., Phys. Rev. Lett. **127**, 175003 (2021).

[11] G. O. Williams, S. Künzel, S. Daboussi, B. Iwan, A. I. Gonzalez, W. Boutu, V. Hilbert, U. Zastrau, H. J. Lee, B. Nagler, et al., Phys. Rev. A **97**, 023414 (2018).

[12] F. Dorchies and V. Recoules, *Non-equilibrium solid-to-plasma transition dynamics using XANES diagnostic* (2016).

[13] P. Corkum and F. Krausz, Nature Physics **3**, 381 (2007).

[14] P. Virtanen, R. Gommers, T. E. Oliphant, M. Haberland, T. Reddy, D. Cournapeau, E. Burovski, P. Peterson, W. Weckesser, J. Bright, et al., Nature Methods **17**, 261 (2020).

[15] M. Hashida, M. Yasuhiro, N. Takaya, S. Mashiro, I. Shunsuke, and S. Shuji, Electronics and Communication in Japan **99**, 88 (2016).

[16] S. I. Anisimov, B. L. Kapeliovich, T. L. Perel'man, and L. D. Landau, Tech. Rep. (1975).

[17] Z. Lin, L. V. Zhigilei, and V. Celli, Physical Review B **77** (2008), ISSN 1098-0121.

[18] B. Rethfeld, A. Kaiser, M. Vicanek, and G. Simon, Physical Review B - Condensed Matter and Materials Physics **65**, 2143031 (2002), ISSN 01631829.

[19] Y. V. Petrov, N. A. Inogamov, and K. P. Migdal, JETP Letters **97** (2013), ISSN 0021-3640.

[20] B. Y. Mueller and B. Rethfeld, Phys. Rev. B **87**, 035139 (2013).

[21] L. Waldecker, R. Bertoni, R. Ernstorfer, and J. Vorberger, Phys. Rev. X **6**, 021003 (2016).

[22] N. Medvedev and I. Milov, Phys. Rev. B **102**, 064302 (2020).

[23] J. F. Seely and E. G. Harris, Phys. Rev. A **7**, 1064 (1973).

[24] N. Hansen, *The cma evolution strategy* (2015).

[25] D. Foreman-Mackey, D. W. Hogg, D. Lang, and J. Goodman, **125**, 306 (2013), 1202.3665.

[26] G. Kresse and J. Hafner, Phys. Rev. B **47**, 558 (1993).

[27] G. Kresse and J. Furthmüller, Computational Materials Science **6**, 15 (1996), ISSN 0927-0256.

[28] G. Kresse and J. Furthmüller, Phys. Rev. B **54**, 11169 (1996).

[29] G. Kresse and J. Hafner, Journal of Physics: Condensed Matter **6**, 8245 (1994).

[30] G. Kresse and D. Joubert, Phys. Rev. B **59**, 1758 (1999).